Applied Mathematics and Computation 219 (2012) 1958–1974

Contents lists available at SciVerse ScienceDirect

Applied Mathematics and Computation

journal homepage: www.elsevier.com/locate/amc

# A local space–time conservation scheme and its application in shock wave propagation

Hua Shen [a,b], Kaixin Liu [a,b,*], Deliang Zhang [c]

[a] LTCS, Department of Mechanics & Aerospace Engineering, College of Engineering, Peking University, Beijing, China
[b] Center for Applied Physics and Technology, Peking University, 100871 Beijing, China
[c] LHD, Institute of Mechanics, Chinese Academy of Science, Beijing, China

ARTICLE INFO

*Keywords:*
Space–time conservation
Non-staggered grids
CE/SE method
Shock wave

ABSTRACT

In this paper, a local space–time conservation scheme based on non-staggered grids is introduced which is a variation of Space–Time Conservation Element and Solution Element (CE/SE) scheme. It inherits most features and advantages of CE/SE method, including unified treatment of space and time, and high-accuracy resolution of hyperbolic conservation equations. Moreover, Riemann solvers are not needed to capture shocks, and dimensional splitting methods are not needed in the multi-dimensional schemes. The stability of the present scheme is verified through von Neumann analysis. Moreover, several shock wave problems including one-, two-, and three-dimensional cases are simulated by the present scheme. By carefully comparing the present scheme's numerical results with exact solutions, experimental results, original CE/SE scheme's numerical results and third-order ENO scheme's numerical results, it can be conclude that, the present scheme is efficient and accurate.



## 1. Introduction

After several decades of development, there are several well-established methods in Computational Fluid Dynamics (CFD), such as finite difference, finite volume, finite element, and spectral methods [1–4]. With the development of science, scientific and engineering problems to be solved become more and more diverse and complex. Traditional numerical methods can not completely meet the needs of science and engineering. In recent years, some new high resolution methods have emerged, such as Boltzmann Gas Kinetics (BGK) [5], Local Discontinuous Galerkin (LDG) [6] and Space–Time Conservation Element and Solution Element (CE/SE) methods [7].

The CE/SE method was originally proposed by Chang and co-workers [7–14] which was a completely new numerical framework for solving hyperbolic conservation equations. This new approach differs substantially in both concept and methodology from the well-established methods. It has many nontraditional features and advantages, including unified treatment of space and time, satisfying both local and global flux conservations in space and time, high accuracy for solving hyperbolic conservation equations, and the simple mathematical treatment. Moreover, Riemann solvers are not needed to capture shocks, and dimensional splitting method is not needed in the multi-dimensional schemes. Theoretical analysis and numerical results demonstrate that the CE/SE method has quite high accuracy and resolution of strong discontinuity [9]. To date, the CE/SE method has achieved great success in simulations of sound wave propagating [11], aero-acoustics [9,15], steady

* Corresponding author at: LTCS, Department of Mechanics & Aerospace Engineering, College of Engineering, Peking University, 100871 Beijing, China.
*E-mail addresses:* shenhua@pku.edu.cn (H. Shen), kliu@pku.edu.cn (K. Liu), dlzhang@imech.ac.cn (D. Zhang).

0096-3003/$ - see front matter © 2012 Elsevier Inc. All rights reserved.
http://dx.doi.org/10.1016/j.amc.2012.08.038

viscous flow [16], complex supersonic flow [17], chemical reactive flow [14,18–20], magneto-hydrodynamics [12], multi-material elastic–plastic flows [21], spall fracture [22] and so on.

In the CE/SE method, the space–time domain to be calculated is divided into non-overlapping conservation elements (CEs) and solution elements (SEs). It is assumed that mesh variables are continuous in each SE, but discontinuities are allowed across the boundaries of neighboring SEs. Taylor series is then used to approximate the mesh variables in SEs. Usually, first-order Taylor series is applied to get a second-order accurate scheme [7], and high-order Taylor series is also applied to get a high-order accurate scheme [23]. Mesh variables are calculated through a local space–time flux balance, which is enforced by integrating over the surfaces of a CE.

It is easy to discover that the CE/SE numerical scheme depends on the definitions of CE and SE. Different definitions of CE and SE lead to different schemes. In Chang's original scheme [7,8], the number of CEs is consistent with the number of unknowns designated by the scheme including the mesh variables and their spatial derivatives. Therefore, two CEs are needed at each grid point to derive two discrete equations for $U$ and $U_x$ in a one-dimensional case. Similarly, three and four CEs are needed at each grid point in two-and three-dimensional cases. Another two different definitions of CE and SE for the two-dimensional case are proposed in Refs. [13,14] and [18–22]. In both of the two methods, only one CE at each grid point is used to calculate the mesh variables, while the spatial derivatives are evaluated by a central differencing method.

In this paper, by adopting the core idea of CE/SE method, a local space–time conservation scheme is constructed based on non-staggered mesh grids in time direction. And it is also extended to genuinely two-and three-dimensional cases without using dimensional splitting methods. Moreover, a theoretical analysis about the present method is investigated. For verifying the resolution and efficiency of the present scheme, it is applied to simulate some shock wave problems. The computational results are also carefully compared with the results from experiments and other literature.

## 2. One-dimensional local space–time conservation scheme

To illustrate the main logic of the present scheme, the construction of the one-dimensional local space–time conservation scheme is introduced at first.

### 2.1. Construction of the numerical scheme

Consider a standard hyperbolic conservation equation

$$\frac{\partial U}{\partial t}+\frac{\partial E(U)}{\partial x}=0. \tag{1}$$

Let $x_1 = x$, and $x_2 = t$ be considered as the coordinates of a two-dimensional Euclidean space $E_2$. Then because Eq. (1) can be expressed as $\nabla\cdot\vec{h}=0$ with $\vec{h}=(E,U)$. Gauss' divergence theorem in the space–time $E_2$ implies that Eq. (1) is the differential form of the integral conservation law

$$\oint_{S(V)}\vec{h}\cdot\vec{ds}=0, \tag{2}$$

where $S(V)$ is the boundary of an arbitrary space–time region $V$ in $E_2$, and $\vec{ds}=d\sigma\vec{n}$ with $d\sigma$ and $\vec{n}$, respectively, being the length and the unit outward normal vector of a boundary segment on $S(V)$.

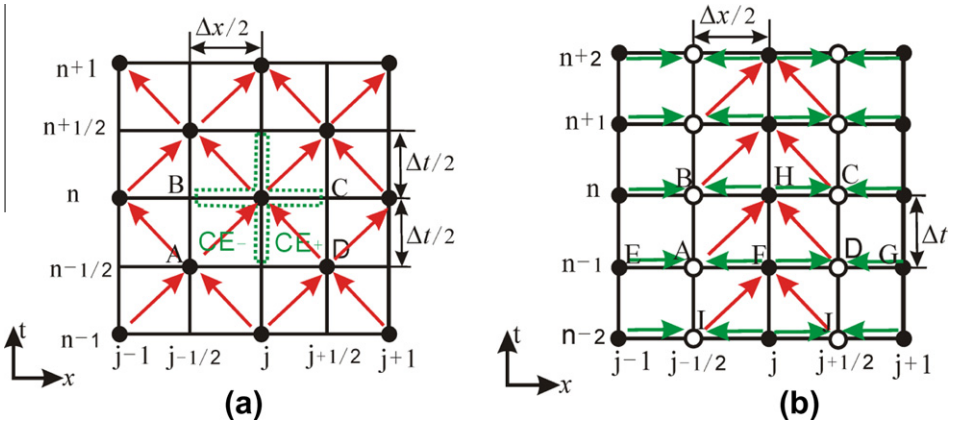


**Fig. 1.** Comparison of space–time mesh grids of the original CE/SE scheme and the present scheme. (a) The staggered mesh grids of space and time and definition of *CE* (rectangle ABCD) and *SE* (the interior of the space–time region bounded by the dashed curve) for the original CE/SE scheme; (b) non-staggered mesh grids of space and time for the present scheme.

To proceed on, the region of space and time is divided into uniform rectangles, as seen in Fig. 1(b). The grid points signed with • are used to store mesh variables and their spatial derivatives. And that signed with ∘ are auxiliary nodes which are mesh grids of neighboring elements in space and time. Obviously, the mesh grids are non-staggered in the time direction. On the contrast, the mesh grids for original CE/SE method are interlaced with each other as shown in Fig. 1(a).

To get a high-order accuracy scheme, the mesh variables and their spatial derivatives at each grid point are calculated separately. Mesh variables are calculated through a local space–time flux balance, which is enforced by integrating Eq. (2) over the surfaces of a space–time element. With respect to rectangle ABCD in Fig. 1(b), the outward unit normal vectors of AB, BC, CD and DA are $(-1,0)$, $(0,1)$, $(1,0)$ and $(0,-1)$. It can be shown that Eq. (2) is equivalent to

$$\oint_{ABCD} \vec{h}\cdot\vec{ds} = -\int_{AB} E(x,t)dt + \int_{BC} U(x,t)dx + \int_{CD} E(x,t)dt - \int_{DA} U(x,t)dx = 0. \tag{3}$$

The form of Eq. (3) depends on the form of $U(x,t)$ and $E(x,t)$ on each boundary line of rectangle ABCD. Here, the simple first-order Taylor series are applied to approximate them, i.e.

$$U^*(x,t;j,n) = (U)_j^n + (U_x)_j^n(x-x_j) + (U_t)_j^n(t-t^n), \tag{4a}$$

$$E^*(x,t;j,n) = (E)_j^n + (E_x)_j^n(x-x_j) + (E_t)_j^n(t-t^n). \tag{4b}$$

Substituting Eqs. (4a) and (4b) into Eq. (1), one gets

$$(U_t)_j^n = -(E_x)_j^n. \tag{5}$$

Eqs. (4) and (5) imply that the variables needed to be calculated are $U$ and $U_x$ at each grid point, because $E$ is a function of $U$.

To construct an explicit scheme, points A, H, D, D and A are consider as the Taylor series' reference points on lines AB, BC, CD, DF and FA. Then Eq. (3) can be written as

$$\begin{aligned} &-\int_{AB}\left[E_{j-\frac{1}{2}}^{n-1} + (E_t)_{j-\frac{1}{2}}^{n-1}(t-t_{n-1})\right]dt + \int_{BC}\left[U_j^n + (U_x)_j^n(x-x_j)\right]dx + \int_{CD}\left[E_{j+\frac{1}{2}}^{n-1} + (E_t)_{j+\frac{1}{2}}^{n-1}(t-t_{n-1})\right]dt \\ &-\int_{DF}\left[U_{j+\frac{1}{2}}^{n-1} + (U_x)_{j+\frac{1}{2}}^{n-1}(x-x_{j+\frac{1}{2}})\right]dx - \int_{FA}\left[U_{j-\frac{1}{2}}^{n-1} + (U_x)_{j-\frac{1}{2}}^{n-1}(x-x_{j-\frac{1}{2}})\right]dx = 0. \end{aligned} \tag{6}$$

Define $S_j^n = \frac{\Delta x}{4}(U_x)_j^n + \frac{2\Delta t}{\Delta x}E_j^n + \frac{\Delta t^2}{\Delta x}(E_t)_j^n$, then Eq. (6) can be reduced to

$$U_j^n = \frac{1}{2}\left[U_{j-\frac{1}{2}}^{n-1} + U_{j+\frac{1}{2}}^{n-1} + S_{j-\frac{1}{2}}^{n-1} - S_{j+\frac{1}{2}}^{n-1}\right], \tag{7}$$

Supposing that mesh variables are continuous in the space time element, the continuous conditions at points B and C imply that

$$U_{j+\frac{1}{2}}^n = U_j^n + (U_x)_j^n\frac{\Delta x}{2} = U_{j+\frac{1}{2}}^{n-1} + (U_t)_{j+\frac{1}{2}}^{n-1}\Delta t, \tag{8a}$$

$$U_{j-\frac{1}{2}}^n = U_j^n - (U_x)_j^n\frac{\Delta x}{2} = U_{j-\frac{1}{2}}^{n-1} + (U_t)_{j-\frac{1}{2}}^{n-1}\Delta t. \tag{8b}$$

According to the two equations, two different values of $(U_x)_j^n$ are derived, i.e.

$$(U_x)_j^{n+} = \frac{2\left(U_{j+\frac{1}{2}}^n - U_j^n\right)}{\Delta x} = \frac{2\left[U_{j+\frac{1}{2}}^{n-1} + (U_t)_{j+\frac{1}{2}}^{n-1}\Delta t - U_j^n\right)}{\Delta x}, \tag{9a}$$

$$(U_x)_j^{n-} = -\frac{2\left(U_{j-\frac{1}{2}}^n - U_j^n\right)}{\Delta x} = -\frac{2\left[U_{j-\frac{1}{2}}^{n-1} + (U_t)_{j-\frac{1}{2}}^{n-1}\Delta t - U_j^n\right)}{\Delta x}. \tag{9b}$$

To evaluate the values of spatial derivatives, we introduce a weighted average function [7] which is defined as

$$W[x_-,x_+,\alpha] = \frac{|x_+|^\alpha x_- + |x_-|^\alpha x_+}{|x_+|^\alpha + |x_-|^\alpha}. \tag{10}$$

Then, the spatial derivative is calculated by

$$(U_x)_j^n = W\left[(U_x)_j^{n+}, (U_x)_j^{n-}, \alpha\right]. \tag{11}$$

If there is no discontinuity, we let $\alpha = 0$. If there are discontinuities, we generally let $\alpha = 1 \sim 2$ [7] to avoid numerical instability.

Another function can instead of the weighted average function, which is defined as [24]

$$\min\text{mod}(x^+,x^-) = \begin{cases} 0 & \text{when } x^+\cdot x^- \leqslant 0, \\ x^+ & \text{when } x^+\cdot x^- > 0 \quad \text{and} \quad |x^+| < |x^-|, \\ x^- & \text{when } x^+\cdot x^- > 0 \quad \text{and} \quad |x^+| > |x^-|. \end{cases} \tag{12}$$

Eqs. (7)–(11) imply that $U_j^n$ and $(U_x)_j^n$ depend on $U_{j-\frac{1}{2}}^{n-1}$, $(U_x)_{j-\frac{1}{2}}^{n-1}$, $U_{j+\frac{1}{2}}^{n-1}$ and $(U_x)_{j+\frac{1}{2}}^{n-1}$ which are the mesh variables and their spatial derivatives on auxiliary nodes. As the finite volume method, different models can be used to evaluate the values of $U$ and $U_x$ on auxiliary nodes to construct different schemes. So the construction of the present scheme can be very flexible. Here we introduce a simple method which is easy to apply in multi-dimensional cases. With respect to $U_{j+\frac{1}{2}}^{n-1}$, $\int_{FG} U(x,t)dx$ is calculated by two ways, i.e.

$$\begin{aligned}\int_{FG} U(x,t)dx &= \int_{x_j}^{x_{j+1}} \left[U_{j+\frac{1}{2}}^{n-1} + (U_x)_{j+\frac{1}{2}}^{n-1}\left(x - x_{j+\frac{1}{2}}\right)\right]dx \\ &= \int_{x_j}^{x_{j+\frac{1}{2}}} \left[U_j^{n-1} + (U_x)_j^{n-1}(x - x_j)\right]dx + \int_{x_{j+\frac{1}{2}}}^{x_{j+1}} \left[U_{j+1}^{n-1} + (U_x)_{j+1}^{n-1}(x - x_{j+1})\right]dx. \end{aligned} \tag{13a}$$

The equation can be reduced to

$$U_{j+\frac{1}{2}}^{n-1} = \frac{1}{2}\left[U_j^{n-1} + (U_x)_j^{n-1}\frac{\Delta x}{4} + U_{j+1}^{n-1} - (U_x)_{j+1}^{n-1}\frac{\Delta x}{4}\right]. \tag{13b}$$

With respect to $(U_x)_{j+\frac{1}{2}}^{n-1}$, it is calculated as $(U_x)_j^n$, i.e.

$$(U_x)_{j+\frac{1}{2}}^{n-1} = W\left[(U_x)_{j+\frac{1}{2}}^{n-1+}, (U_x)_{j+\frac{1}{2}}^{n-1-}, \alpha\right], \tag{14}$$

where, $(U_x)_{j+\frac{1}{2}}^{n-1-} = -\frac{2(U_j^{n-1} - U_{j+\frac{1}{2}}^{n-1})}{\Delta x}$, $(U_x)_{j+\frac{1}{2}}^{n-1+} = \frac{2(U_{j+1}^{n-1} - U_{j+\frac{1}{2}}^{n-1})}{\Delta x}$.

The present scheme has been constructed by Eqs. 7, 11, 13a and 14. It implies that $U$ and $U_x$ at $(j,n)$ can be calculated through $U$ and $U_x$ at $(j-1,n-1)$, $(j,n-1)$ and $(j+1,n-1)$. So the present scheme is a three point explicit scheme. It follows most methodology of the CE/SE method, except the staggered mesh grids. It is worth mentioning that the global flux conservation is not fully satisfied in the time direction in the present scheme, because two different ways are used to calculate $\int_{AD} U(x,t)dx$ when calculate $U_F$ and $U_H$. The flux may not completely vanish through the rectangle BIJC. But in global space and local space–time region, flux conservation is satisfied perfectly.

### 2.2. von Neumann analysis

To illustrate the effectiveness of the present scheme, von Neumann analysis has been done. Let $U = u$ and $E(U) = au$ in Eq. (1). Thus, Eq. (1) is equivalent to the simple one-dimensional convection equation

$$\frac{\partial u}{\partial t} + a\frac{\partial u}{\partial x} = 0, \tag{15}$$

where the advection speed $a \neq 0$ is a constant. Here, the case with no discontinuity ($\alpha = 0$) is considered. Let $v = a\frac{\Delta t}{\Delta x}$. Thus, Eqs. 7, 13b, 11 and 14 are equivalent to

$$u_j^n = \frac{1}{2}\left[(1+2v)u_{j-\frac{1}{2}}^{n-1} + (1-2v)u_{j+\frac{1}{2}}^{n-1}\right] + \frac{\Delta x}{8}(1-4v^2)\left[(u_x)_{j-\frac{1}{2}}^{n-1} - (u_x)_{j+\frac{1}{2}}^{n-1}\right], \tag{16a}$$

$$u_{j+\frac{1}{2}}^{n-1} = \frac{1}{2}\left[u_j^{n-1} + (u_x)_j^{n-1}\frac{\Delta x}{4} + u_{j+1}^{n-1} - (u_x)_{j+1}^{n-1}\frac{\Delta x}{4}\right], \tag{16b}$$

$$(u_x)_j^n = W\left[(u_x)_j^{n+}, (u_x)_j^{n-}, 0\right] = \frac{u_{j+\frac{1}{2}}^{n-1} - v(u_x)_{j+\frac{1}{2}}^{n-1}\Delta x - u_{j-\frac{1}{2}}^{n-1} + v(u_x)_{j-\frac{1}{2}}^{n-1}\Delta x}{\Delta x}, \tag{16c}$$

$$(u_x)_{j+\frac{1}{2}}^{n-1} = W\left[(u_x)_{j+\frac{1}{2}}^{n-1+}, (u_x)_{j+\frac{1}{2}}^{n-1-}, 0\right] = \frac{u_{j+1}^{n-1} - u_j^{n-1}}{\Delta x}. \tag{16d}$$

Eqs. (16a)–(16d) can be expressed in matrix form, i.e.

$$q_j^n = M_+ q_{j-\frac{1}{2}}^{n-1} + M_- q_{j+\frac{1}{2}}^{n-1}, \tag{17a}$$

$$q_{j+\frac{1}{2}}^{n-1} = M_1 q_j^{n-1} + M_2 q_{j+1}^{n-1}. \tag{17b}$$

Here

$$q_j^n = \left(u_j^n, (u_x)_j^n \Delta x\right),$$

$$M_+ = \frac{1}{2}\begin{bmatrix} 1+2v & \frac{1}{4}-v^2 \\ -2 & 2v \end{bmatrix}, \quad M_- = \frac{1}{2}\begin{bmatrix} 1-2v & -\frac{1}{4}+v^2 \\ 2 & -2v \end{bmatrix},$$

$$M_1 = \frac{1}{2}\begin{bmatrix} 1 & \frac{1}{4} \\ -2 & 0 \end{bmatrix}, \quad M_2 = \frac{1}{2}\begin{bmatrix} 1 & -\frac{1}{4} \\ 2 & 0 \end{bmatrix}.$$

Substituting Eq. (17b) into Eqs. (17a), (17a) is equivalent to

$$q_j^n = M_+M_1q_{j-1}^{n-1} + M_+M_2q_j^{n-1} + M_-M_1q_j^{n-1} + M_-M_2q_{j+1}^{n-1}. \tag{18}$$

Let $q_j^n = q^*(n,\theta)e^{ij\theta}(-\pi \leqslant \theta < \pi, e^{i\theta} = \cos\theta + i\sin\theta)$, then Eq. (18) is equivalent to

$$q^*(n,\theta) = Mq^*(n-1,\theta). \tag{19}$$

Here

$$M = \left(M_+e^{-i\frac{\theta}{2}} + M_-e^{i\frac{\theta}{2}}\right)\left(M_1e^{-i\frac{\theta}{2}} + M_2e^{i\frac{\theta}{2}}\right),$$

i.e.

$$M = \begin{bmatrix} 1-\left(v^2+\frac{1}{4}\right)(1-\cos\theta) - iv\sin\theta & -\frac{v}{4}(1-\cos\theta) - i\frac{1}{8}\sin\theta \\ 2v(1-\cos\theta) + i\sin\theta & \frac{1}{4}(1-\cos\theta) \end{bmatrix}.$$

The characteristic function of matrix **M** is

$$\lambda^2 - [1 - v^2(1-\cos\theta) - iv\sin\theta]\lambda + \frac{1}{4}(1-\cos\theta) + \frac{1}{4}\left(v^2 - \frac{1}{4}\right)(1-\cos\theta)^2 - \frac{1}{8}\sin^2\theta + i\frac{v}{4}\sin\theta(1-\cos\theta) = 0. \tag{20}$$

Assuming that $\lambda_1$ and $\lambda_2$ are the roots of Eq. (20), define the function $f(v,\theta) = \max(|\lambda_1|,|\lambda_2|)(0 < v < 1, -\pi \leqslant \theta \leqslant \pi)$. Because the roots of Eq. (20) are too complex to derive its theoretical solution, numerical calculation is used to solve it. The variation of $f(v,\theta)$ with respect to $v$ and $\theta$ is shown in Fig. 2.

The white plane in Fig. 2 is $f = 1$. Numerical results show that, the value of function $f(v,\theta)$ is always smaller than 1.0 when $v \leqslant 0.43$. But the value of function $f(v,\theta)$ is very close to 1.0 near $v = 0.5$. And note that, von Neumann stability condition is $\rho(M) = \max(|\lambda_1|,|\lambda_2|) \leqslant 1 + K\Delta t$. On the right side of inequality, $K\Delta t$ is a small term. So the stability condition can be relaxed appropriately. Actually, when $v \leqslant 0.52$, the function $f(v,\theta)$ is always smaller than 1.01. Thus, the stability condition is considered as $0 < v \leqslant 0.52$ which is consistent with the numerical stability condition.

Note that, for the specific case $v = 0$, Eq. (18) reduces to

$$q_j^n = \begin{bmatrix} \frac{1}{8} & \frac{1}{16} \\ -\frac{1}{2} & -\frac{1}{8} \end{bmatrix} q_{j-1}^{n-1} + \begin{bmatrix} \frac{3}{4} & 0 \\ 0 & \frac{1}{4} \end{bmatrix} q_j^{n-1} + \begin{bmatrix} \frac{1}{8} & -\frac{1}{16} \\ \frac{1}{2} & -\frac{1}{8} \end{bmatrix} q_{j+1}^{n-1}. \tag{21}$$

Because $v \to 0$ as $\Delta t \to 0$, Eq. (21) implies that $q_j^n$ does not approach to $q_j^{n-1}$ as $\Delta t \to 0$. Because (i) point $(j,n)$ would approach point $(j,n-1)$ when $\Delta t \to 0$, and (ii) both points (j,n) and (j,n-1) are the mesh points where solution variables are stored and marked by solid circles in Fig. 1(b), this implies that the present scheme fails to satisfy the accuracy requirement that the solution variables at the mesh point $(j,n)$ should approach those stored at the mesh point $(j,\ n-1)$ as these two approach each other in the limit of $\Delta t \to 0$. This failure would lead to the conclusion that the present scheme is highly dissipative in the limit of $v \to 0$. With respect to the shock wave propagation problems, the present scheme is accuracy and efficient when the Courant number is not too small. To solve a problem with large Courant number disparity, the present scheme need to be further improved. A family of very robust Courant number insensitive CE/SE scheme has been developed [10].

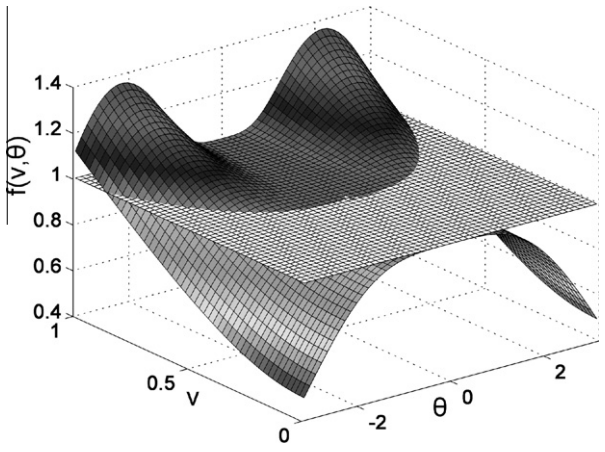


**Fig. 2.** Variation of $f(v,\theta)$ with respect to $v$ and $\theta$.

## 3. Multi-dimensional schemes

In order to further improve the algorithm, it is necessary to extended it to multi-dimensional cases. As mentioned above, in the present scheme, dimensional splitting method is not needed in the multi-dimensional schemes. The logic of multi-dimensional schemes is simple and almost the same as the one-dimensional scheme. First, the three-dimensional scheme is constructed carefully. Then the two-dimensional scheme is supplied generally.

### 3.1. The three-dimensional scheme

Consider a standard three-dimensional hyperbolic conservation equation

$$\frac{\partial U}{\partial t}+\frac{\partial E(U)}{\partial x}+\frac{\partial F(U)}{\partial y}+\frac{\partial G(U)}{\partial z}=0. \tag{22}$$

Here, let $x_1=x$, $x_2=y$, $x_3=z$ and $x_4=t$ be the coordinates of a four-dimensional Euclidean space $E_4$. In Eq. (2), $\vec{h}=(E,F,G,U)$. $S(V)$ is the boundary of an arbitrary space–time region $V$ in $E_4$, and $\vec{ds}=d\sigma\vec{n}$ with $d\sigma$ and $\vec{n}$, respectively, being the volume and the unit outward normal vector of a surface element on $S(V)$.

To proceed on, the whole space is divided into uniform hexahedrons. A typical spatial mesh element is shown in Fig. 3(a). V1–V8 are the eight vertices of the hexahedron which are used to store mesh variables and their spatial derivatives. The central point of hexahedron V1V2V3V4V5V6V7V8 A1 is an auxiliary node. C1–C6 and B1–B12 are the central points of the six faces and the twelve edges of the hexahedron. A four-dimensional space–time element is shown in Fig. 3(b). Points V1–V8 are at time level $t=t^n$. Points V1′–V8′ are the corresponding points at time level $t=t^{n+1}$. Hereto forth, the above rule is applied to all points for denoting the time level, i.e., the superscript $'$ for points at time level $t=t^{n+1}$, and none for points at $t=t^n$. Obviously, the mesh grids are non-staggered in the time direction.

Suppose that the integral conservation laws are satisfied in the space–time element shown in Fig. 3(b). Note that the boundaries of the space–time element are hexahedrons A1′A2′A3′A4′A5′A6′A7′A8′, A1A2A3A4A5A6A7A8, A2A3A7A6A2′A3′A7′A6′, A1A4A8A5A1′A4′A8′A5′, A3A4A8A7A3′A4′A8′A7′, A1A2A6A5A1′A2′A6′A5′, A5A6A7A8A5′A6′A7′A8′ and A1A2A3A4A1′A2′A3′A4′ whose outward unit normal vectors are $(0,0,0,1)$, $(0,0,0,-1)$, $(1,0,0,0)$, $(-1,0,0,0)$, $(0,1,0,0)$, $(0,-1,0,0)$, $(0,0,1,0)$ and $(0,0,-1,0)$. Under these conditions, Eq. (2) is equivalent to

$$\begin{aligned}\iiint_{S(V)}\vec{h}\cdot\vec{ds}=&\iiint_{A1'A2'A3'A4'A5'A6'A7'A8'}Udxdydz-\iiint_{A1A2A3A4A5A6A7A8}Udxdydz+\iiint_{A2A3A7A6A2'A3'A7'A6'}Edydzdt\\&-\iiint_{A1A4A8A5A1'A4'A8'A5'}Edydzdt+\iiint_{A3A4A8A7A3'A4'A8'A7'}Fdxdzdt-\iiint_{A1A2A6A5A1'A2'A6'A5'}Fdxdzdt\\&+\iiint_{A5A6A7A8A5'A6'A7'A8'}Gdxdydt-\iiint_{A1A2A3A4A1'A2'A3'A4'}Gdxdydt=0.\end{aligned} \tag{23}$$

With the aid of first order Taylor expansions at the reference points A1, A2, A3, A4, A5, A6, A7, A8 and V7′, we have

$$\iiint_{A1'A2'A3'A4'A5'A6'A7'A8'}Udxdydz=U_{V7'}\Delta x\Delta y\Delta z, \tag{24a}$$

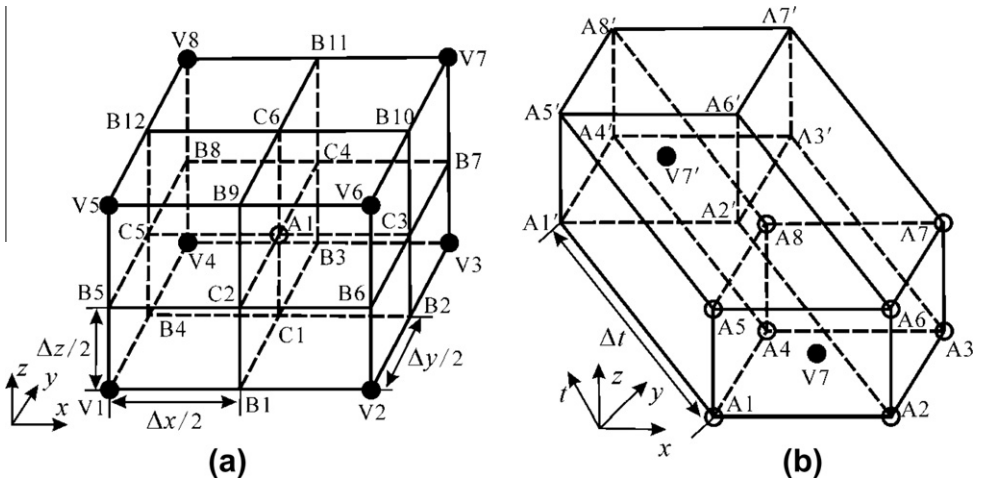


**Fig. 3.** Schematic of the computational mesh grids for the three-dimensional scheme. (a) Three-dimensional spatial mesh grids; (b) the space–time element.

$$\iiint_{A1A2A3A4A5A6A7A8} U dxdydz = \frac{\Delta x\Delta y\Delta z}{8}\left[U\left(\frac{\Delta x}{4},\frac{\Delta y}{4},\frac{\Delta z}{4},0\right)_{A1} + U\left(-\frac{\Delta x}{4},\frac{\Delta y}{4},\frac{\Delta z}{4},0\right)_{A2} + U\left(-\frac{\Delta x}{4},-\frac{\Delta y}{4},\frac{\Delta z}{4},0\right)_{A3} + U\left(\frac{\Delta x}{4},-\frac{\Delta y}{4},\frac{\Delta z}{4},0\right)_{A4} + U\left(\frac{\Delta x}{4},\frac{\Delta y}{4},-\frac{\Delta z}{4},0\right)_{A5} + U\left(-\frac{\Delta x}{4},\frac{\Delta y}{4},-\frac{\Delta z}{4},0\right)_{A6} + U\left(-\frac{\Delta x}{4},-\frac{\Delta y}{4},-\frac{\Delta z}{4},0\right)_{A7} + U\left(\frac{\Delta x}{4},-\frac{\Delta y}{4},-\frac{\Delta z}{4},0\right)_{A8}\right], \tag{24b}$$

$$\iiint_{A2A3A7A6A2'A3'A7'A6'} E dydzdt = \frac{\Delta y\Delta z\Delta t}{4}\left[E\left(0,\frac{\Delta y}{4},\frac{\Delta z}{4},\frac{\Delta t}{2}\right)_{A2} + E\left(0,-\frac{\Delta y}{4},\frac{\Delta z}{4},\frac{\Delta t}{2}\right)_{A3} + E\left(0,-\frac{\Delta y}{4},-\frac{\Delta z}{4},\frac{\Delta t}{2}\right)_{A7} + E\left(0,\frac{\Delta y}{4},-\frac{\Delta z}{4},\frac{\Delta t}{2}\right)_{A6}\right], \tag{24c}$$

$$\iiint_{A1A4A8A5A1'A4'A8'A5'} E dydzdt = \frac{\Delta y\Delta z\Delta t}{4}\left[E\left(0,\frac{\Delta y}{4},\frac{\Delta z}{4},\frac{\Delta t}{2}\right)_{A1} + E\left(0,-\frac{\Delta y}{4},\frac{\Delta z}{4},\frac{\Delta t}{2}\right)_{A4} + E\left(0,-\frac{\Delta y}{4},-\frac{\Delta z}{4},\frac{\Delta t}{2}\right)_{A8} + E\left(0,\frac{\Delta y}{4},-\frac{\Delta z}{4},\frac{\Delta t}{2}\right)_{A5}\right], \tag{24d}$$

$$\iiint_{A3A4A8A7A3'A4'A8'A7'} F dxdzdt = \frac{\Delta x\Delta z\Delta t}{4}\left[F\left(-\frac{\Delta x}{4},0,\frac{\Delta z}{4},\frac{\Delta t}{2}\right)_{A3} + F\left(\frac{\Delta x}{4},0,\frac{\Delta z}{4},\frac{\Delta t}{2}\right)_{A4} + F\left(\frac{\Delta x}{4},0,-\frac{\Delta z}{4},\frac{\Delta t}{2}\right)_{A8} + F\left(-\frac{\Delta x}{4},0,-\frac{\Delta z}{4},\frac{\Delta t}{2}\right)_{A7}\right], \tag{24e}$$

$$\iiint_{A1A2A6A5A1'A2'A6'A5'} F dxdzdt = \frac{\Delta x\Delta z\Delta t}{4}\left[F\left(\frac{\Delta x}{4},0,\frac{\Delta z}{4},\frac{\Delta t}{2}\right)_{A1} + F\left(-\frac{\Delta x}{4},0,\frac{\Delta z}{4},\frac{\Delta t}{2}\right)_{A2} + F\left(-\frac{\Delta x}{4},0,-\frac{\Delta z}{4},\frac{\Delta t}{2}\right)_{A6} + F\left(\frac{\Delta x}{4},0,-\frac{\Delta z}{4},\frac{\Delta t}{2}\right)_{A5}\right] \tag{24f}$$

$$\iiint_{A5A6A7A8A5'A6'A7'A8'} G dxdydt = \frac{\Delta x\Delta y\Delta t}{4}\left[G\left(\frac{\Delta x}{4},\frac{\Delta y}{4},0,\frac{\Delta t}{2}\right)_{A5} + G\left(-\frac{\Delta x}{4},\frac{\Delta y}{4},0,\frac{\Delta t}{2}\right)_{A6} + G\left(-\frac{\Delta x}{4},-\frac{\Delta y}{4},0,\frac{\Delta t}{2}\right)_{A7} + G\left(\frac{\Delta x}{4},-\frac{\Delta y}{4},0,\frac{\Delta t}{2}\right)_{A8}\right], \tag{24g}$$

$$\iiint_{A1A2A3A4A1'A2'A3'A4'} G dxdydt = \frac{\Delta x\Delta y\Delta t}{4}\left[G\left(\frac{\Delta x}{4},\frac{\Delta y}{4},0,\frac{\Delta t}{2}\right)_{A1} + G\left(-\frac{\Delta x}{4},\frac{\Delta y}{4},0,\frac{\Delta t}{2}\right)_{A2} + G\left(-\frac{\Delta x}{4},-\frac{\Delta y}{4},0,\frac{\Delta t}{2}\right)_{A3} + G\left(\frac{\Delta x}{4},-\frac{\Delta y}{4},0,\frac{\Delta t}{2}\right)_{A4}\right]. \tag{24h}$$

Substituting Eqs. (24a)–(24h) into Eq. (23), the three-dimensional numerical scheme is constructed as

$$U_{V7'} = \frac{1}{8}\left(\overline{U} + 2\frac{\Delta t}{\Delta x}\overline{E} + 2\frac{\Delta t}{\Delta y}\overline{F} + 2\frac{\Delta t}{\Delta z}\overline{G}\right), \tag{25}$$

where,

$$\overline{U} = U\left(\frac{\Delta x}{4},\frac{\Delta y}{4},\frac{\Delta z}{4},0\right)_{A1} + U\left(-\frac{\Delta x}{4},\frac{\Delta y}{4},\frac{\Delta z}{4},0\right)_{A2} + U\left(-\frac{\Delta x}{4},-\frac{\Delta y}{4},\frac{\Delta z}{4},0\right)_{A3} + U\left(\frac{\Delta x}{4},-\frac{\Delta y}{4},\frac{\Delta z}{4},0\right)_{A4} + U\left(\frac{\Delta x}{4},\frac{\Delta y}{4},-\frac{\Delta z}{4},0\right)_{A5} + U\left(-\frac{\Delta x}{4},\frac{\Delta y}{4},-\frac{\Delta z}{4},0\right)_{A6} + U\left(-\frac{\Delta x}{4},-\frac{\Delta y}{4},-\frac{\Delta z}{4},0\right)_{A7} + U\left(\frac{\Delta x}{4},-\frac{\Delta y}{4},-\frac{\Delta z}{4},0\right)_{A8}, \tag{26a}$$

$$\overline{E} = E\left(0,\frac{\Delta y}{4},\frac{\Delta z}{4},\frac{\Delta t}{2}\right)_{A1} - E\left(0,\frac{\Delta y}{4},\frac{\Delta z}{4},\frac{\Delta t}{2}\right)_{A2} - E\left(0,-\frac{\Delta y}{4},\frac{\Delta z}{4},\frac{\Delta t}{2}\right)_{A3} + E\left(0,-\frac{\Delta y}{4},\frac{\Delta z}{4},\frac{\Delta t}{2}\right)_{A4} + E\left(0,\frac{\Delta y}{4},-\frac{\Delta z}{4},\frac{\Delta t}{2}\right)_{A5} - E\left(0,\frac{\Delta y}{4},-\frac{\Delta z}{4},\frac{\Delta t}{2}\right)_{A6} - E\left(0,-\frac{\Delta y}{4},-\frac{\Delta z}{4},\frac{\Delta t}{2}\right)_{A7} + E\left(0,-\frac{\Delta y}{4},-\frac{\Delta z}{4},\frac{\Delta t}{2}\right)_{A8}, \tag{26b}$$

$$\overline{F} = F\left(\frac{\Delta x}{4},0,\frac{\Delta z}{4},\frac{\Delta t}{2}\right)_{A1} + F\left(-\frac{\Delta x}{4},0,\frac{\Delta z}{4},\frac{\Delta t}{2}\right)_{A2} - F\left(-\frac{\Delta x}{4},0,\frac{\Delta z}{4},\frac{\Delta t}{2}\right)_{A3} - F\left(\frac{\Delta x}{4},0,\frac{\Delta z}{4},\frac{\Delta t}{2}\right)_{A4} + F\left(\frac{\Delta x}{4},0,-\frac{\Delta z}{4},\frac{\Delta t}{2}\right)_{A5} + F\left(-\frac{\Delta x}{4},0,-\frac{\Delta z}{4},\frac{\Delta t}{2}\right)_{A6} - F\left(-\frac{\Delta x}{4},0,-\frac{\Delta z}{4},\frac{\Delta t}{2}\right)_{A7} - F\left(\frac{\Delta x}{4},0,-\frac{\Delta z}{4},\frac{\Delta t}{2}\right)_{A8}, \tag{26c}$$

$$\overline{G} = G\left(\frac{\Delta x}{4}, \frac{\Delta y}{4}, 0, \frac{\Delta t}{2}\right)_{A1} + G\left(-\frac{\Delta x}{4}, \frac{\Delta y}{4}, 0, \frac{\Delta t}{2}\right)_{A2} + G\left(-\frac{\Delta x}{4}, -\frac{\Delta y}{4}, 0, \frac{\Delta t}{2}\right)_{A3} + G\left(\frac{\Delta x}{4}, -\frac{\Delta y}{4}, 0, \frac{\Delta t}{2}\right)_{A4} - G\left(\frac{\Delta x}{4}, \frac{\Delta y}{4}, 0, \frac{\Delta t}{2}\right)_{A5} - G\left(-\frac{\Delta x}{4}, \frac{\Delta y}{4}, 0, \frac{\Delta t}{2}\right)_{A6} - G\left(-\frac{\Delta x}{4}, -\frac{\Delta y}{4}, 0, \frac{\Delta t}{2}\right)_{A7} - G\left(\frac{\Delta x}{4}, -\frac{\Delta y}{4}, 0, \frac{\Delta t}{2}\right)_{A8}. \tag{26d}$$

Here $X(dx, dy, dz, dt)_N$ are the Taylor expansions of $U,\ E,\ F$ and $G$ at the reference point $N$, i.e.

$$X(dx, dy, dz, dt)_N = X_N + (X_x)_N dx + (X_y)_N dy + (X_z)_N dz + (X_t)_N dt. \tag{27}$$

Substituting Eq. (27) into Eq. (22), we obtain

$$(U_t)_N = -(E_x)_N - (F_y)_N - (G_z)_N. \tag{28}$$

Eqs. (27) and (28) imply that the variables needed to be calculated are $U,\ U_x,\ U_y$, and $U_z$ at each grid point, because $E,\ F$ and $G$ are functions of $U$.

Suppose that mesh variables are continuous in the space–time element. The continuous condition at points A1′, A2′, A3′, A4′, A5′, A6′, A7′ and A8′ imply that

$$U_{A1'} = U_{A1} + \Delta t(U_t)_{A1} = U_{V7'} - (U_x)_{V7'}\frac{\Delta x}{2} - (U_y)_{V7'}\frac{\Delta y}{2} - (U_z)_{V7'}\frac{\Delta z}{2}, \tag{29a}$$

$$U_{A2'} = U_{A2} + \Delta t(U_t)_{A2} = U_{V7'} + (U_x)_{V7'}\frac{\Delta x}{2} - (U_y)_{V7'}\frac{\Delta y}{2} - (U_z)_{V7'}\frac{\Delta z}{2}, \tag{29b}$$

$$U_{A3'} = U_{A3} + \Delta t(U_t)_{A3} = U_{V7'} + (U_x)_{V7'}\frac{\Delta x}{2} + (U_y)_{V7'}\frac{\Delta y}{2} - (U_z)_{V7'}\frac{\Delta z}{2}, \tag{29c}$$

$$U_{A4'} = U_{A4} + \Delta t(U_t)_{A4} = U_{V7'} - (U_x)_{V7'}\frac{\Delta x}{2} + (U_y)_{V7'}\frac{\Delta y}{2} - (U_z)_{V7'}\frac{\Delta z}{2}, \tag{29d}$$

$$U_{A5'} = U_{A5} + \Delta t(U_t)_{A5} = U_{V7'} - (U_x)_{V7'}\frac{\Delta x}{2} - (U_y)_{V7'}\frac{\Delta y}{2} + (U_z)_{V7'}\frac{\Delta z}{2}, \tag{29e}$$

$$U_{A6'} = U_{A6} + \Delta t(U_t)_{A6} = U_{V7'} + (U_x)_{V7'}\frac{\Delta x}{2} - (U_y)_{V7'}\frac{\Delta y}{2} + (U_z)_{V7'}\frac{\Delta z}{2}, \tag{29f}$$

$$U_{A7'} = U_{A7} + \Delta t(U_t)_{A7} = U_{V7'} + (U_x)_{V7'}\frac{\Delta x}{2} + (U_y)_{V7'}\frac{\Delta y}{2} + (U_z)_{V7'}\frac{\Delta z}{2}, \tag{29g}$$

$$U_{A8'} = U_{A8} + \Delta t(U_t)_{A8} = U_{V7'} - (U_x)_{V7'}\frac{\Delta x}{2} + (U_y)_{V7'}\frac{\Delta y}{2} + (U_z)_{V7'}\frac{\Delta z}{2}. \tag{29h}$$

By adding Eqs. (29a), (29d), (29e) and (29h), Eqs. (29b), (29c), (29f) and (29g), Eqs. (29a), (29b), (29e) and (29f), Eqs. (29c), (29d), (29g) and (29h), Eqs. (29a)–(29d) and Eqs. (29e)–(29h) together, two different values of each spatial derivatives are derived, i.e.

$$(U_x)^{-}_{V7'} = -\frac{1}{2\Delta x}[U(0,0,0,\Delta t)_{A1} + U(0,0,0,\Delta t)_{A4} + U(0,0,0,\Delta t)_{A5} + U(0,0,0,\Delta t)_{A8} - 4U_{V7'}], \tag{30a}$$

$$(U_x)^{+}_{V7'} = +\frac{1}{2\Delta x}[U(0,0,0,\Delta t)_{A2} + U(0,0,0,\Delta t)_{A3} + U(0,0,0,\Delta t)_{A6} + U(0,0,0,\Delta t)_{A7} - 4U_{V7'}], \tag{30b}$$

$$(U_y)^{-}_{V7'} = -\frac{1}{2\Delta y}[U(0,0,0,\Delta t)_{A1} + U(0,0,0,\Delta t)_{A2} + U(0,0,0,\Delta t)_{A5} + U(0,0,0,\Delta t)_{A6} - 4U_{V7'}], \tag{30c}$$

$$(U_y)^{+}_{V7'} = +\frac{1}{2\Delta y}[U(0,0,0,\Delta t)_{A3} + U(0,0,0,\Delta t)_{A4} + U(0,0,0,\Delta t)_{A7} + U(0,0,0,\Delta t)_{A8} - 4U_{V7'}], \tag{30d}$$

$$(U_z)^{-}_{V7'} = -\frac{1}{2\Delta z}[U(0,0,0,\Delta t)_{A1} + U(0,0,0,\Delta t)_{A2} + U(0,0,0,\Delta t)_{A3} + U(0,0,0,\Delta t)_{A4} - 4U_{V7'}], \tag{30e}$$

$$(U_z)^{+}_{V7'} = +\frac{1}{2\Delta z}[U(0,0,0,\Delta t)_{A5} + U(0,0,0,\Delta t)_{A6} + U(0,0,0,\Delta t)_{A7} + U(0,0,0,\Delta t)_{A8} - 4U_{V7'}]. \tag{30f}$$

Following the previous practice, the spatial derivatives are calculated as

$$\begin{aligned}(U_x)_{V7'} &= W\left[(U_x)^{-}_{V7'}, (U_x)^{+}_{V7'}, \alpha\right]\\ (U_y)_{V7'} &= W\left[(U_y)^{-}_{V7'}, (U_y)^{+}_{V7'}, \alpha\right]\\ (U_z)_{V7'} &= W\left[(U_z)^{-}_{V7'}, (U_z)^{+}_{V7'}, \alpha\right]\end{aligned} \tag{31}$$

Eqs. (25)–(31) imply that $U,\ U_x,\ U_y$, and $U_z$ at V7′ are calculated by $U,\ U_x,\ U_y$, and $U_z$ at auxiliary nodes A1, A2, A3, A4, A5, A6, A7 and A8. Respect to $U_{A1}$, two ways are used to calculate $\iiint_{V1V2V3V4V5V6V7V8} U dxdydz$, i.e.

$$\begin{aligned}\iiint_{\mathrm{V1V2V3V4V5V6V7V8}} U dxdydz = &\iiint_{\mathrm{V1B1C1B4B5C2A1C5}} U dxdydz + \iiint_{\mathrm{B1V2B2C1C2B6C3A1}} U dxdydz \\ &+ \iiint_{\mathrm{C1B2V3B3A1C3B7C4}} U dxdydz + \iiint_{\mathrm{B4C1B3V4C5A1C4B8}} U dxdydz \\ &+ \iiint_{\mathrm{B5C2A1C5V5B9C6B12}} U dxdydz + \iiint_{\mathrm{C2B6C3A1B9V6B10C6}} U dxdydz \\ &+ \iiint_{\mathrm{A1C3B7C4C6B10V7B11}} U dxdydz + \iiint_{\mathrm{C5A1C4B8B12C6B11V8}} U dxdydz. \end{aligned} \tag{32}$$

Eq. (32) can be reduced to

$$\begin{aligned} U_{\mathrm{A1}} = \frac{1}{8}\Big[ &U\left(\frac{\Delta x}{4},\frac{\Delta y}{4},\frac{\Delta z}{4},0\right)_{\mathrm{V1}} + U\left(-\frac{\Delta x}{4},\frac{\Delta y}{4},\frac{\Delta z}{4},0\right)_{\mathrm{V2}} + U\left(-\frac{\Delta x}{4},-\frac{\Delta y}{4},\frac{\Delta z}{4},0\right)_{\mathrm{V3}} + U\left(\frac{\Delta x}{4},-\frac{\Delta y}{4},\frac{\Delta z}{4},0\right)_{\mathrm{V4}} \\ &+ U\left(\frac{\Delta x}{4},\frac{\Delta y}{4},-\frac{\Delta z}{4},0\right)_{\mathrm{V5}} + U\left(-\frac{\Delta x}{4},\frac{\Delta y}{4},-\frac{\Delta z}{4},0\right)_{\mathrm{V6}} + U\left(-\frac{\Delta x}{4},-\frac{\Delta y}{4},-\frac{\Delta z}{4},0\right)_{\mathrm{V7}} + U\left(\frac{\Delta x}{4},-\frac{\Delta y}{4},-\frac{\Delta z}{4},0\right)_{\mathrm{V8}}\Big]. \end{aligned} \tag{33}$$

With respect to the spatial derivatives at A1, they can be evaluated by using the continuous condition at points V1, V2, V3, V4, V5, V6, V7 and V8. The detailed process is almost the same with the calculation of $U_x$, $U_y$ and $U_z$ at V7′. The final results are

$$\begin{aligned} (U_x)_{A1} &= W\left[(U_x)^-_{\mathrm{A1}}, (U_x)^+_{\mathrm{A1}}, \alpha\right], \\ (U_y)_{A1} &= W\left[(U_y)^-_{\mathrm{A1}}, (U_y)^+_{\mathrm{A1}}, \alpha\right], \\ (U_z)_{A1} &= W\left[(U_z)^-_{\mathrm{A1}}, (U_z)^+_{\mathrm{A1}}, \alpha\right]. \end{aligned} \tag{34}$$

Here

$$\begin{aligned} (U_x)^+_{\mathrm{A1}} &= \frac{U_{\mathrm{V2}} + U_{\mathrm{V3}} + U_{\mathrm{V6}} + U_{\mathrm{V7}} - 4U_{\mathrm{A1}}}{2\Delta x}, \\ (U_x)^-_{\mathrm{A1}} &= -\frac{U_{\mathrm{V1}} + U_{\mathrm{V4}} + U_{\mathrm{V5}} + U_{\mathrm{V8}} - 4U_{\mathrm{A1}}}{2\Delta x}, \\ (U_y)^+_{\mathrm{A1}} &= \frac{U_{\mathrm{V3}} + U_{\mathrm{V4}} + U_{\mathrm{V7}} + U_{\mathrm{V8}} - 4U_{\mathrm{A1}}}{2\Delta y}, \\ (U_y)^-_{\mathrm{A1}} &= -\frac{U_{\mathrm{V1}} + U_{\mathrm{V2}} + U_{\mathrm{V5}} + U_{\mathrm{V6}} - 4U_{\mathrm{A1}}}{2\Delta y}, \\ (U_z)^+_{\mathrm{A1}} &= \frac{U_{\mathrm{V5}} + U_{\mathrm{V6}} + U_{\mathrm{V7}} + U_{\mathrm{V8}} - 4U_{\mathrm{A1}}}{2\Delta z}, \\ (U_z)^-_{\mathrm{A1}} &= -\frac{U_{\mathrm{V1}} + U_{\mathrm{V2}} + U_{\mathrm{V3}} + U_{\mathrm{V4}} - 4U_{\mathrm{A1}}}{2\Delta z}. \end{aligned}$$

### 3.2. The two-dimensional scheme

With respect to the two-dimensional case, the whole space is divided into uniform rectangles as seen in Fig. 4(a). The vertices of the rectangles V1, V2, V3, V4, V5, V6, V7, V8 and V9 signed with • are the grid points used to store mesh variables

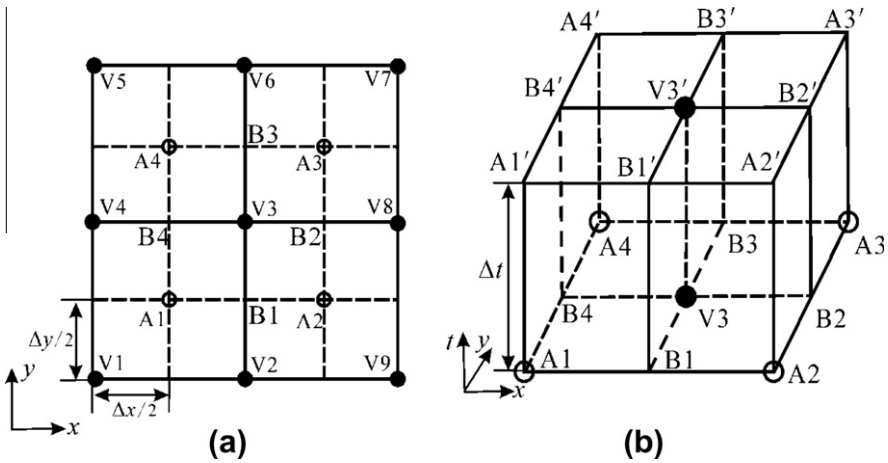


**Fig. 4.** Schematic of the computational mesh grids for the two-dimensional scheme. (a) Two-dimensional spatial mesh grids; (b) the space–time element.

and their spatial derivatives. The center points of the rectangles A1, A2, A3 and A4 signed with ◦ are auxiliary nodes. B1–B4 are the central points of the four edges of rectangle A1A2A3A4. Fig. 4(b) shows a typical element in space and time. The same rule as the three-dimensional case is applied to all points for denoting the time level.

The whole process of the construction is similar with the construction of the three-dimensional scheme. There is just a little difference. That is all the volume integrals are replaced by area integrals. So the detailed process is not repeated, just the final scheme is supplied as follows.

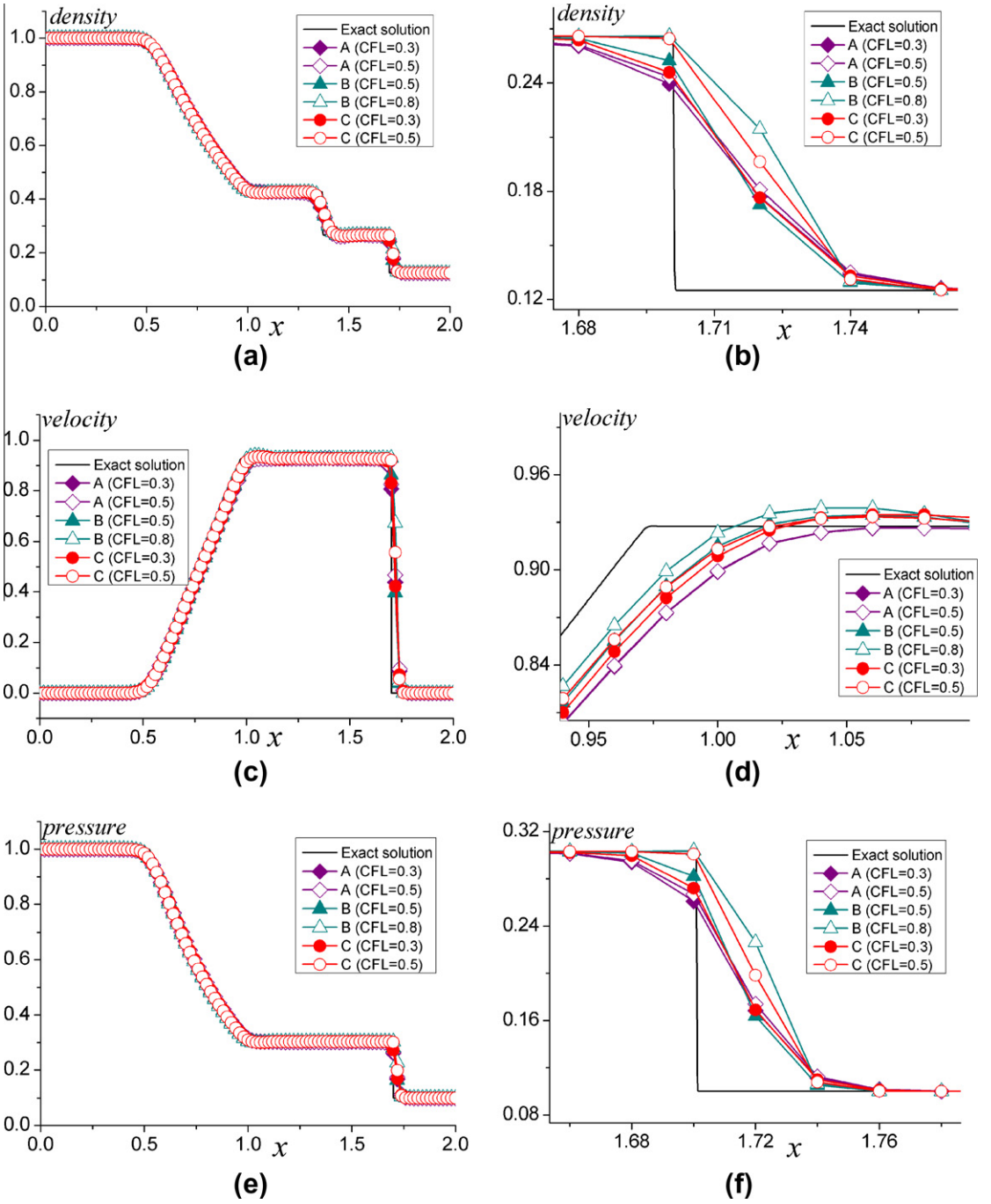


**Fig. 5.** Comparison of numerical results at $t = 0.4$ derived by three numerical schemes. A, B and C represent the third-order ENO scheme, the original CE/SE scheme and the present scheme. (a) Density distribution of the whole $x$ axis; (b) local enlargement of the density distribution; (c) velocity distribution of the whole $x$ axis; (d) local enlargement of the velocity distribution; (e) pressure distribution of the whole $x$ axis; (f) local enlargement of the pressure distribution.

Mesh variables at grid points are calculated by

$$U_{V3'} = \frac{1}{4}\left(\overline{U} + 2\frac{\Delta t}{\Delta x}\overline{E} + 2\frac{\Delta t}{\Delta y}\overline{F}\right), \tag{35}$$

where

$$\begin{aligned}
\overline{U} &= U\left(\frac{\Delta x}{4}, \frac{\Delta y}{4}, 0\right)_{A1} + U\left(-\frac{\Delta x}{4}, \frac{\Delta y}{4}, 0\right)_{A2} + U\left(-\frac{\Delta x}{4}, -\frac{\Delta y}{4}, 0\right)_{A3} + U\left(\frac{\Delta x}{4}, -\frac{\Delta y}{4}, 0\right)_{A4},\\
\overline{E} &= E\left(0, \frac{\Delta y}{4}, \frac{\Delta t}{2}\right)_{A1} - E\left(0, \frac{\Delta y}{4}, \frac{\Delta t}{2}\right)_{A2} - E\left(0, -\frac{\Delta y}{4}, \frac{\Delta t}{2}\right)_{A3} + E\left(0, -\frac{\Delta y}{4}, \frac{\Delta t}{2}\right)_{A4},\\
\overline{F} &= F\left(\frac{\Delta x}{4}, 0, \frac{\Delta t}{2}\right)_{A1} + F\left(-\frac{\Delta x}{4}, 0, \frac{\Delta t}{2}\right)_{A2} - F\left(-\frac{\Delta x}{4}, 0, \frac{\Delta t}{2}\right)_{A3} - F\left(\frac{\Delta x}{4}, 0, \frac{\Delta t}{2}\right)_{A4}.
\end{aligned}$$

Spatial derivatives at grid points are calculated by

$$\begin{aligned}
(U_x)_{V3'} &= W\left[(U_x)^-_{V3'}, (U_x)^+_{V3'}, \alpha\right],\\
(U_y)_{V3'} &= W\left[(U_y)^-_{V3'}, (U_y)^+_{V3'}, \alpha\right],
\end{aligned} \tag{36}$$

where

$$\begin{aligned}
(U_x)^+_{V3'} &= \frac{U(0,0,\Delta t)_{A2} + U(0,0,\Delta t)_{A3} - 2U_{V3'}}{\Delta x},\\
(U_x)^-_{V3'} &= -\frac{U(0,0,\Delta t)_{A1} + U(0,0,\Delta t)_{A4} - 2U_{V3'}}{\Delta x},\\
(U_y)^+_{V3'} &= \frac{U(0,0,\Delta t)_{A3} + U(0,0,\Delta t)_{A4} - 2U_{V3'}}{\Delta y},\\
(U_y)^-_{V3'} &= -\frac{U(0,0,\Delta t)_{A1} + U(0,0,\Delta t)_{A2} - 2U_{V3'}}{\Delta y}.
\end{aligned}$$

Mesh variables at auxiliary nodes are calculated by

$$U_{A1} = \frac{1}{4}\left[U\left(\frac{\Delta x}{4}, \frac{\Delta y}{4}, 0\right)_{V1} + U\left(-\frac{\Delta x}{4}, \frac{\Delta y}{4}, 0\right)_{V2} + U\left(-\frac{\Delta x}{4}, -\frac{\Delta y}{4}, 0\right)_{V3} + U\left(\frac{\Delta x}{4}, -\frac{\Delta y}{4}, 0\right)_{V4}\right]. \tag{37}$$

Spatial derivatives at auxiliary nodes are calculated by

$$\begin{aligned}
(U_x)_{A1} &= W\left[(U_x)^-_{A1}, (U_x)^+_{A1}, \alpha\right],\\
(U_y)_{A1} &= W\left[(U_y)^-_{A1}, (U_y)^+_{A1}, \alpha\right],
\end{aligned} \tag{38}$$

where

$$\begin{aligned}
(U_x)^+_{A1} &= \frac{U_{V2} + U_{V3} - 2U_{A1}}{\Delta x},\\
(U_x)^-_{A1} &= -\frac{U_{V1} + U_{V4} - 2U_{A1}}{\Delta x},\\
(U_y)^+_{A1} &= \frac{U_{V3} + U_{V4} - 2U_{A1}}{\Delta y},\\
(U_y)^-_{A1} &= -\frac{U_{V1} + U_{V2} - 2U_{A1}}{\Delta y}.
\end{aligned}$$

## 4. Numerical examples

To demonstrate the capabilities of the present 1D, 2D and 3D schemes, we apply them to solve Euler equations. For three-dimensional unsteady Euler equations of a prefect gas, $U$, $E$, $F$ and $G$ in Eq. (22) are defined as

$$U = \begin{bmatrix} \rho \\ \rho u \\ \rho v \\ \rho w \\ e \end{bmatrix}, \quad E = \begin{bmatrix} \rho u \\ \rho u^2 + p \\ \rho uv \\ \rho uw \\ (e+p)u \end{bmatrix}, \quad F = \begin{bmatrix} \rho v \\ \rho uv \\ \rho v^2 + p \\ \rho vw \\ (e+p)v \end{bmatrix}, \quad G = \begin{bmatrix} \rho w \\ \rho uw \\ \rho vw \\ \rho w^2 + p \\ (e+p)w \end{bmatrix}, \tag{39}$$

where $\rho$ is the density, $u$, $v$ and $w$ are the velocity components of $x$-direction, $y$-direction and $z$-direction respectively, $p$ is the pressure, and $e$ is the total energy per unit volume. Consider the fluid as a perfect gas, $e$ can be calculated by the following equation

$$e = \frac{p}{\gamma - 1} + \frac{1}{2}\rho(u^2 + v^2 + w^2). \tag{40}$$

### 4.1. One-dimensional shock tube problem

First, a shock tube problem suggested by Sod [25] is considered. The shock tube is filled with perfect gas. The gas is divided into two parts by a diaphragm placed at $x = 1$. The gas state at $t = 0$ is

$$(\rho, u, p) = \begin{cases} (1.0, 0, 1.0) & 0 \leqslant x \leqslant 1 \\ (0.125, 0, 0.1) & 1 < x \leqslant 2 \end{cases}. \tag{41}$$

When computation starts, the diaphragm vanishes instantly. Non-reflecting boundary conditions are imposed on both sides of the tube. To test the one dimensional local space–time conservation scheme, the results are compared with that calculated by third-order ENO scheme [26,27] and original CE/SE scheme [7]. All the numerical results are derived by dividing the whole one-dimensional space into 100 uniform line segments. Because the present scheme and the original CE/SE scheme are sensitive with the CFL number and have a parameter $\alpha$, different CFL numbers and the same $\alpha(\alpha = 2)$ are considered.

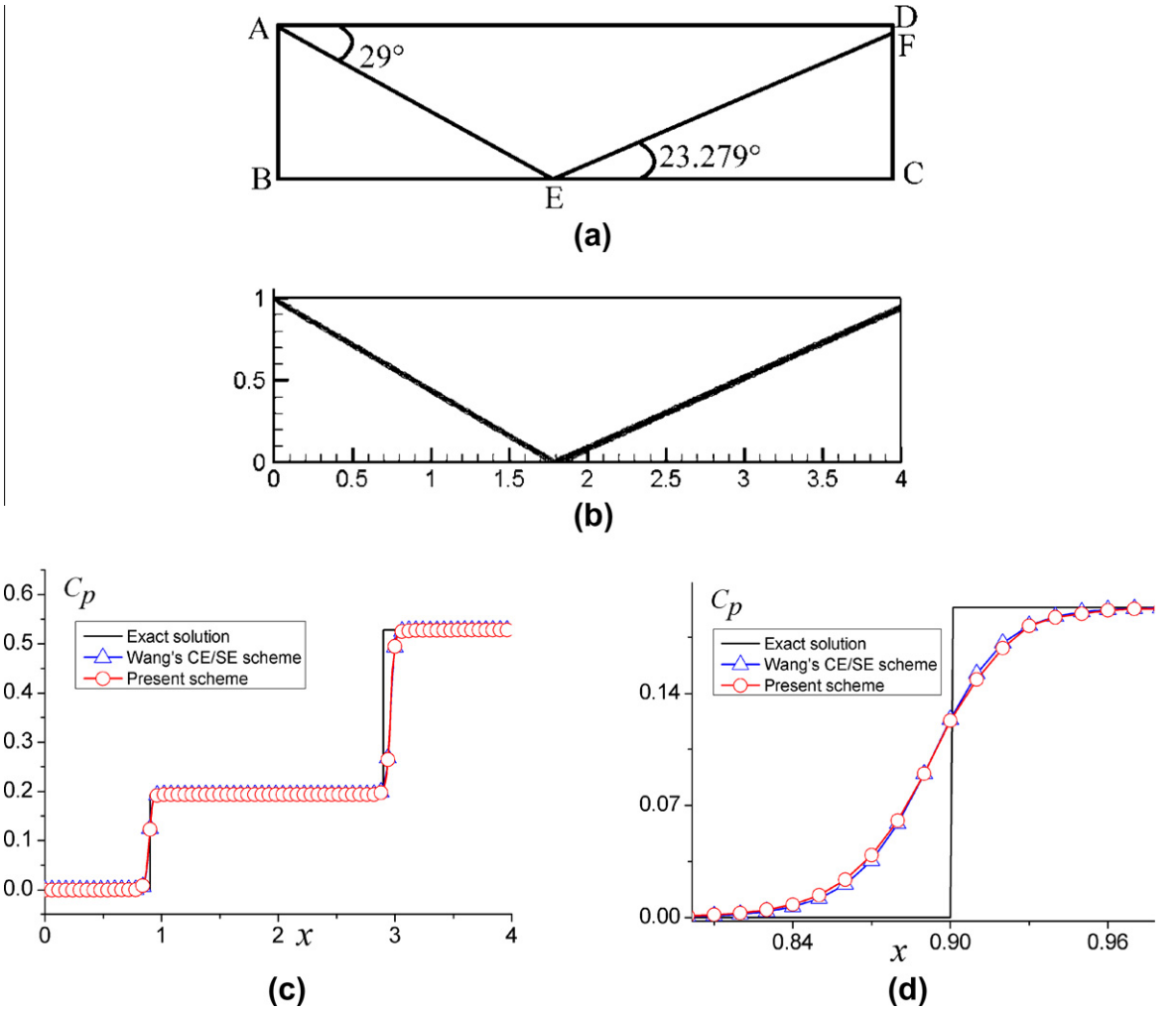


**Fig. 6.** Comparison of numerical results and the exact solution for the shock reflection on a plate. (a) Schematic of the exact solution; (b) density contours calculated by present scheme (401 × 101); (c) pressure coefficient distribution of the whole $x$ axis at the mid-section of the computation domain (y = 0.5); (d) local enlargement of pressure coefficient distribution.

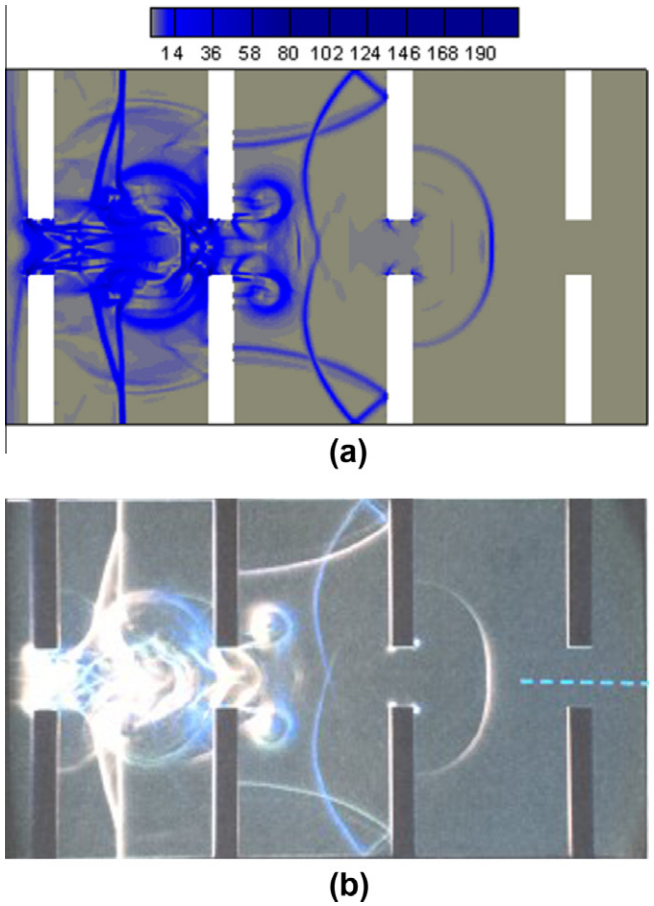


**Fig. 7.** Comparison of the numerical result and experimental photographs at $t = 1.05$. (a) The numerical result; (b) the corresponding experimental photographs.

Fig. 5 shows that all the three schemes' accuracy is very high. Numerical results are very close to exact solution just calculated by 101 mesh grids. Local enlargement figures imply that the present scheme and the original CE/SE scheme's results are closer to exact solution than third-order ENO scheme's result. When CFL=0.5, the present scheme's result is the best. When the Courant number is smaller (CFL=0.3), the present scheme becomes more dissipative. The results agree with the theoretical analysis in Section 2.2.

### 4.2. Shock reflection on a flat plate

This steady-state test problem was proposed by Yee et al. [28]. By imposing suitable upstream conditions, oblique incident and reflected shocks will appear above a flat plate. The spatial computational domain is a $4.0 \times 1.0$ rectangle.

The flow conditions at $t = 0$ are [13]

$$(\rho, u, v, p) = \begin{cases} (1.0, 2.9, 0.0, 0.71428) & \text{ahead of the incident shock,} \\ (1.7, 2.6193, -0.50632, 1.5282) & \text{behind the incident shock.} \end{cases} \tag{42}$$

For $t > 0$, (i) the flow conditions given in the first and second rows on the right side of Eq. (42) are imposed on the left and the top boundaries, respectively; (ii) the reflecting boundary conditions are imposed on the bottom boundary (a solid wall); and (iii) the nonreflecting conditions are imposed on the right boundary (a supersonic outlet).

Fig. 6(b) shows the density contours computed by the present 2D scheme with $\alpha = 1$ and CFL=0.4, which agrees with the exact solution (Fig. 6(a)) well. In order to evaluate accuracy of the present scheme further, the shock reflection problem is also calculated under the same conditions by Wang's CE/SE scheme [19]. Fig. 6(c) shows the distribution of the pressure coefficient $C_p$ $\left(C_p = \frac{2\left(\frac{p}{p_\infty} - 1\right)}{\gamma M_\infty^2}\right)$ [19] at y=0.5 by the two numerical schemes, and the exact solution is also provided. Fig. 6(d) gives a local enlargement vision of the pressure coefficient. It shows that the accuracy of the present scheme is equivalent to Wang's

CE/SE scheme. According to Wang's results, his improved CE/SE scheme's accuracy is higher than first-order Roe scheme and second-order MUSCL scheme [19]. So it is concluded that the present two-dimensional scheme retains high accuracy.

### 4.3. Shock wave passes a tunnel with clapboards

To test the 2D scheme further, a more complex problem is considered. The computational domain is a $1.68\times0.93$ rectangle. There are eight $0.06\times0.39$ clapboards placed at the bottom and top of the tunnel at $x = 0.072,\ x = 0.54,\ x = 1.008$ and $x = 1.476$. At $t = 0$, a planar incident shock (Ms = 1.41) is placed at the entrance and the flow conditions in the tunnel are $(\rho, u, v, p) = (1.4, 0, 0, 1.0)$. The whole domain is meshed by $561\times311$ grids.

For $t > 0$, (i) the flow conditions calculated by the normal shock condition are imposed on the left boundary; (ii) the reflecting boundary conditions are imposed on the top and bottom boundaries and the boundaries of the clapboards (a solid wall); and (iii) the nonreflecting conditions are imposed on the right boundary (a supersonic outlet).

When the shock passes the tunnel, normal shock reflections, oblique shock reflections and vortexes generate and interact with each other. Thus, the flow becomes very complex. To enhance the visual effect, the spatial derivative of density $\left(\sqrt{\rho_x^2+\rho_y^2}\right)$ is used to capture the shock waves. The numerical results at $t$ =1.05 compared with experimental photographs

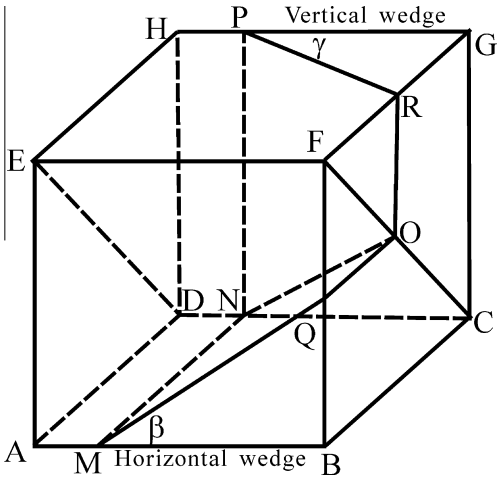


**Fig. 8.** Schematic of computational domain for the shock wave reflection over two intersecting wedges.

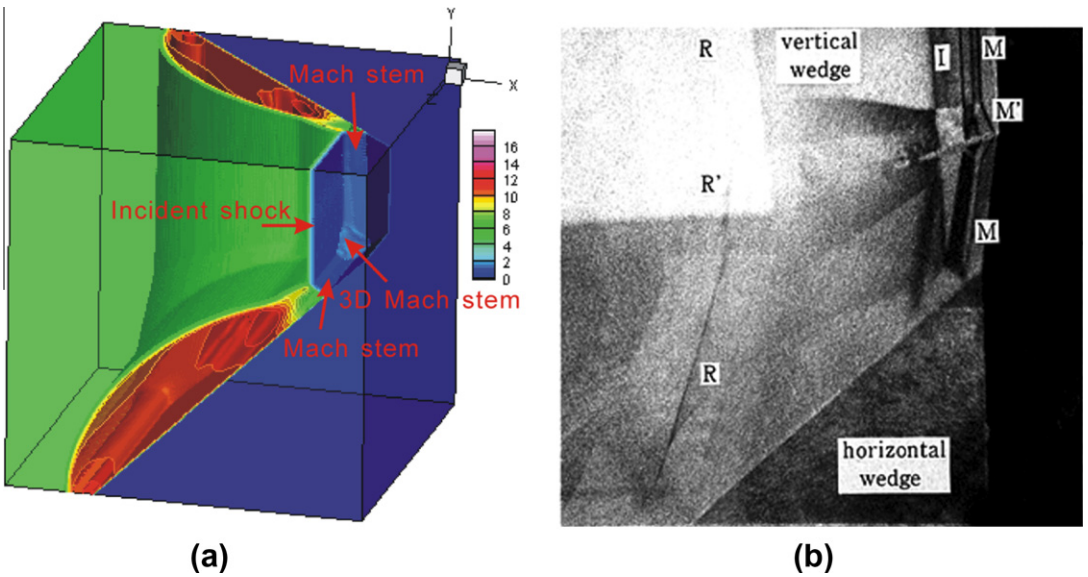


**Fig. 9.** Comparison of the numerical result and experimental photographs at $t$ = 0.6 for the shock wave reflection over two intersecting wedges. (a) The numerical result; (b) the corresponding experimental photograph.

[29] are presented in Fig. 7(a) and (b). These results show that the numerical result agrees well with the experimental result except for some subtle differences. The reasons causing these differences are the experimental conditions in Ref. [29] are not illustrated clearly and the resolution of the film used in the experiment is limited. Moreover, the computation is based on Euler equations, so those phenomena induced by the viscous effect are not captured. This case suggests that the present 2D scheme can simulate complex flow accurately.

### 4.4. Shock wave reflection over two intersecting wedges

As shown in Fig. 8, the whole computational domain is a $2.0 \times 2.0 \times 2.0$ cube including a horizontal wedge and a vertical wedge, where AM = 0.5. ON is the intersecting line of the two wedges. The inclination angles of the two wedges are $\beta$ and $\gamma$. The flow conditions at $t = 0$ are $(\rho, u, v, w, p) = (1.4, 0, 0, 0, 1.0)$. A planar incident shock is placed at plane ADEH. The whole domain is divided into $200 \times 200 \times 200$ uniform hexahedrons including the two wedges. Here, the numerical and experimental [30] results with $\beta = 45^\circ$, $\gamma = 45^\circ$ and Ms = 2.85 are supplied in Fig. 9(a) and (b).

For $t > 0$, (i) the flow conditions calculated by the normal shock condition are imposed on the left boundary (plane ADHE); (ii) the nonreflecting conditions are imposed on the right boundary (plane FQOR); (iii) the reflecting boundary conditions are imposed on the other boundaries (planes AEFQM, AMND, DNPH, EFRPH, PNOR and MNOQ).

Theoretical and experimental results show that, when the inclination angle of the wedge or the strength of incident shock is different, the reflection pattern is different in a two-dimensional case. There are four different patterns on the whole, including double Mach reflection, single Mach reflection, transitional Mach reflection and regular reflection. In Fig. 10(a),

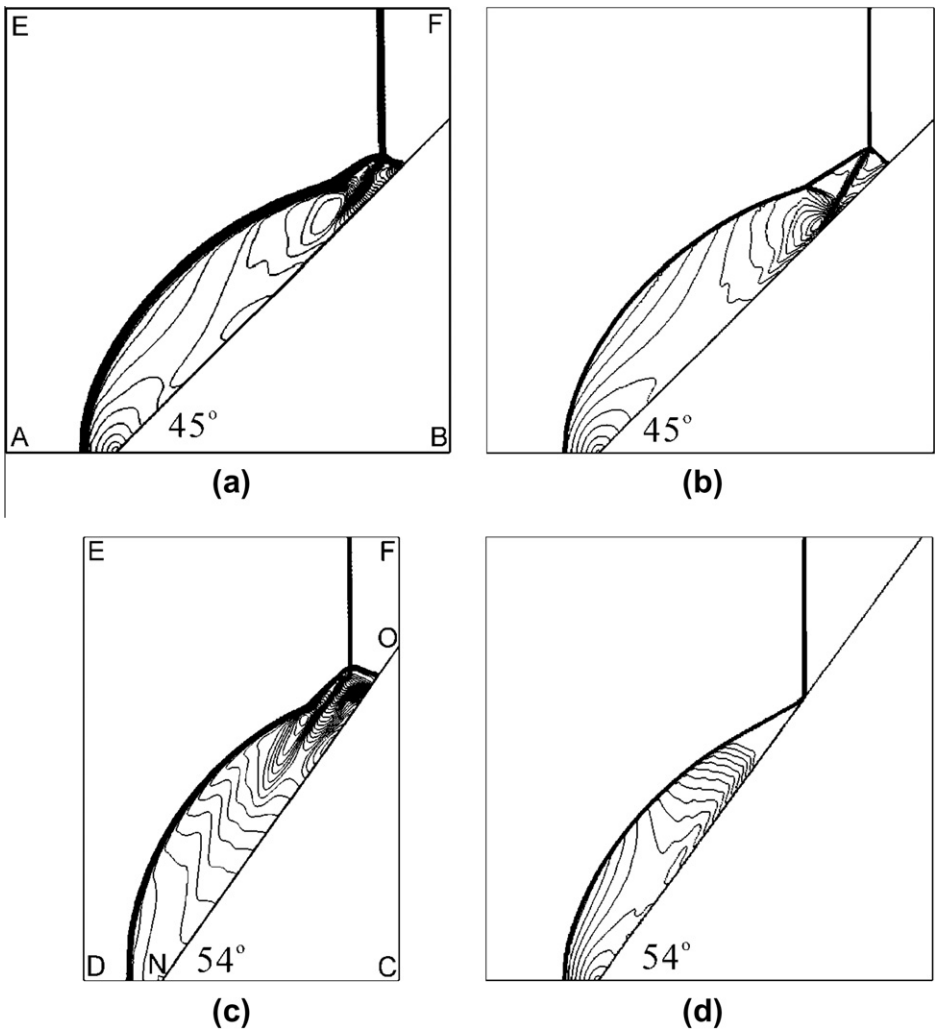


**Fig. 10.** Comparison of the two-and three-dimensional numerical results. (a) The reflection pattern on plane ABFE; (b) the two-dimensional reflection pattern over a 45° wedge; (c) the reflection pattern on plane CDEF; (d) the two-dimensional reflection pattern over a 54° wedge.

the density contours on plane ABFE show a double Mach reflection over a 45° wedge. It is consistent with the two-dimensional numerical results as shown in Fig. 10(b). This case agrees with Ben-Dor's [31] research in two-dimensional cases. Since the two Mach stems interact with each other perpendicularly, a 3D Mach stem generate near the intersecting line of the two wedges. As a result, the density contours on plane CDEF also show a double Mach reflection over a 54° (When $\beta = 45^\circ$ and $\gamma = 45^\circ$, the intersecting line ON lies on the plane CDEF. $\angle CNO = \arctan\sqrt{2} \simeq 54^\circ$) wedge, as shown in Fig. 10(c). But at the 54° wedge angle and Ms = 2.85, it should be a regular reflection according to Ben-Dor's research, as shown in Fig. 10(d). Comparing Fig. 10(c) and (d), the pattern of Mach reflection on plane CDEF is a little different from that in a two dimensional case. A wall jet is generated along the line of the two intersecting wedges. It makes the Mach stem lean forward near the line of the two intersecting wedges. A further study about this problem is available in Ref. [30].

## 5. Concluding Remarks

This paper introduces a local space–time conservation scheme based on non-staggered mesh grids, which is a variation of CE/SE method. This method retains local flux conservation in space and time and global flux conservation in space. It is proved that the present scheme has many good features theoretically and practically: (a) Space and time is treated uniformly; (b) Mathematical treatment is very simple. Dimensional splitting method is not used in the constructions of two- and three-dimensional schemes. Riemann solver is not needed to capture shocks. Only a simple weighted average function is considered as a limiter to calculate the spatial gradients; (c) Through the numerical examples, it can be seen that the present scheme has a good ability to capture the complex structure of the flow including diffraction, reflection, Mach stems, complex vortexes and their interactions.

In future work, several extensions of the present scheme will be developed including a Courant number insensitive scheme and a scheme for unstructured mesh grids.

## Acknowledgements

The authors gratefully acknowledge the financial support of the National Natural Science Foundation of China (Grant Nos. 10732010, 10972010 and 11028206).

## References

[1] T.D. Taylor, R. Peyret, Computational Methods for Fluid Flow, Springer-Verlag, 1983.
[2] G.A. Sod, Numerical Methods in Fluid Dynamics, Cambridge University Press, Cambridge, 1985.
[3] M.D. Su, S.Y. Huang, The Basis of Computational Fluid Dynamics (in Chinese), Tsinghua University Press, 1997.
[4] O.C. Zienkiewicz, R.L. Taylor, The Finite Element Method Fluid Dynamic, fifth ed., vol. 3, Butterworth-Heinemann, 2000.
[5] K. Xu, L. Martinelli, A. Jamson, Gas-kinetic finite volume methods, fulx-vector splitting, and artificial diffusion, J. Comput. Phys. 120 (1) (1995) 48–65.
[6] B. Cockburn, C.W. Shu, The local discontinuous galerkin method for time-dependent convection-diffusion systems, SIAM J. Numer. Anal. 35 (6) (1998) 2440–2463.
[7] S.C. Chang, The method of space-time conservation element and solution element-a new approach for solving the Navier–Stokes and Euler equations, J. Comput. Phys. 119 (1995) 295–324.
[8] S.C. Chang, X.Y. Wang, C.Y. Chow, The space-time conservation element and solution element method: a new high-resolution and genuinely multidimensional paradigm for solving conservation laws, J. Comput. Phys. 156 (1999) 89–136.
[9] X.Y. Wang, S.C. Chang, P.C.E. Jorgenson, Accuracy study of the space-time CE/SE method for computational aero-acoustics problems involving shock waves, AIAA (2000). 2000-0475.
[10] S.C. Chang, X.Y. Wang, Multi-dimensional courant number insensitive CE/SE euler solvers for applications involving highly nonuniform meshes, AIAA (2003) 2003–5280.
[11] X.Y. Wang, S.C. Chang, P.C.E. Jorgenson, Prediction of sound waves propagating through a nozzle without/with a shock wave using the space-time CE/SE method, AIAA (2000). 2000-0222.
[12] M.J. Zhang, S.T. John Yu, S.C. Henry Lin, S.C. Chang, Isaiah Blankson, Solving the MHD equations by the space-time conservation and solution element method, J. Comput. Phys. 214 (2006) 599–617.
[13] Z.C. Zhang, S.T. John Yu, S.C. Chang, A space-time conservation element and solution element method for solving the two-and three-dimensional unsteady Euler equations using quadrilateral and hexahedral meshes, J. Comput. Phys. 175 (2002) 168–199.
[14] Z.C. Zhang, S.T. John Yu, H. He, S.C. Chang, Direct calculations of two-and three-dimensional detonations by an extended CESE method, AIAA (2001). 2001-0476.
[15] M. Liu, J.B. Wang, K.Q. Wu, The direct aero-acoustics simulation of flow around a square cylinder using the CE/SE scheme, J. Algorithms Comput. Technol. 1 (4) (2007) 525–537.
[16] Y.H. Guo, A.T. Hsu, J. Wu, Z.G. Yang, A. Oyediran, Extension of CE/SE method to 2D viscous flows, Comput. Fluids 33 (2004) 1349–1361.
[17] B.S. Venkatachari, Y. Ito, G. Cheng, C.L. Chang, Numerical investigation of the interaction of counterflowing jets an supersonic capsule flows, AIAA (2011) 2011–4030.
[18] G. Wang, D.L. Zhang, K.X. Liu, An improved CE/SE scheme and its application to detonation propagation, Chin. Phys. Lett. 24 (2007) 3563–3566.
[19] G. Wang, D.L. Zhang, K.X. Liu, J.T. Wang, An improved CE/SE scheme for numerical simulation of gaseous and two-phase detonations, Comput. Fluids 39 (2010) 168–177.
[20] G. Wang, D.L. Zhang, K.X. Liu, Numerical study on critical wedge angle of cellular detonation reflections, Chin. Phys. Lett. 27 (2010) 024701.
[21] J.T. Wang, K.X. Liu, D.L. Zhang, A new CE/SE scheme for multi-material elastic-plastic flow and its application, Comput. Fluids 38 (2009) 544–551.
[22] Q.Y. Chen, J.T. Wang, K.X. Liu, Improved CE/SE scheme with particle level set method for numerical simulation of spall fracture due to high-velocity impact, J. Comput. Phys. 29 (2010) 7503–7519.
[23] K.X. Liu, J.T. WANG, Analysis of high accuracy conservation element and solution element schemes, Chin. Phys. Lett. 21 (2004) 2085–2088.
[24] Z.C. Zhang, S.T. John Yu, A non-oscillatory central scheme for conservation laws, AIAA (1999) 99–3576.
[25] G.A. Sod, A survey of several finite difference methods for systems of non-linear hyperbolic conservation laws, J. Comput. Phys. 27 (1978) 1–31.
[26] A. Harten, ENO schemes with sub-cell resolution, J. Comput. Phys. 83 (1980) 148–184.
[27] A. Harten, S. Osher, Uniformly high order accurate essentially non-oscillatory schemes, I, SIAM J. Numer. Anal. 68 (1987) 151–179.

[28] H.C. Yee, R.F. Warming, A. Harten, Implicit Total Variation Diminishing (TVD) Scheme for Steady-State Calculations, AIAA Technical Paper 1902 (AIAA Press, Washington DC, 1983).
[29] P. Krehl, S. Engemann, P. Neuwald, Flash lighting instrumentation for color schlieren shock wave photograph, Shock Waves 4 (1995) 194–207.
[30] T. Meguro, K. Takayama, O. Onodera, Three-dimensional shock wave reflection over a corner of two intersecting wedges, Shock Waves 7 (1997) 107–121.
[31] G. Ben-Dor, Glass II non-stationary oblique shock wave reflections: actual isopycnics and numerical experiments, AIAA J. 16 (1978) 1146–1153.